We are IntechOpen, the world's leading publisher of Open Access books Built by scientists, for scientists

4,800
Open access books available

122,000
International authors and editors

135M
Downloads

Our authors are among the

154
Countries delivered to

TOP 1%
most cited scientists

12.2%
Contributors from top 500 universities

WEB OF SCIENCE™

Selection of our books indexed in the Book Citation Index in Web of Science™ Core Collection (BKCI)

Interested in publishing with us?
Contact book.department@intechopen.com

Numbers displayed above are based on latest data collected.
For more information visit www.intechopen.com

4

Numerical Simulation of High-Power Operation of 2 μm Co-doped Tm,Ho Solid-State Lasers

O. A. Louchev[1], Y. Urata[1], M. Yumoto[2], N. Saito[2] and S. Wada[2]
[1]*Megaopto Co. Ltd., RIKEN Cooperation Center W414, 2-1 Hirosawa, Wako, Saitama 351-0106,*
[2]*Solid-State Optical Science Research Unit, RIKEN, 2-1 Hirosawa, Wako, Saitama 351-0198,*
[1,2]*Japan*

1. Introduction

The development of solid state 2 μm Tm, Ho lasers has remained a topic of particular interest for many years, due to a number of possible applications such as coherent laser radar, atmospheric sensing, a possible pump source for an optical parametric oscillator operating in the mid-infrared region, and medicine. In recent years significant progress in understanding the basic phenomena underlying Tm,Ho laser operation as well as in developing high power lasers has been achieved (Tyminski *et al*., 1989; French *et al*., 1992; Petrin *et al*., 1992; Jani *et al*., 1991; Jani *et al*., 1995; Yu *et al*., 1998; Alpat'ev *et al*., 1998; Alpat'ev *et al*., 1993; Barnes *et al*., 1996; Lee *et al*., 1996; Rustad & Stenersen, 1996; Bruneau, 1998; Bourdet & Lescroart, 1999; Jackson & King, 1998; Sudesh & Asai, 2003; Sato *et al*., 2004; Walsh *et al*. 2004; Galzerano *et al*., 2004; Izawa *et al*., 2000; Yu *et al*., 2006; Zhang *et al*. 2006; Louchev *et al*. 2007 and 2008) and recently reviewed by (Eichhorn, 2008) and (Walsh, 2009). Nevertheless significant effort is still necessary for defining optimized parameters and achieving high lasing efficiency for high power operation associated with significant temperature increase and related effects of pulse energy inhibition and thermal lensing destroying laser operation (Akhmanov *et al.* 1972).

In this work we review main computational and numerical optimization results of a side pumped Tm,Ho:YLF laser for producing MW-power giant pulses with durations of several hundred nanoseconds using the coupled thermo-optical model (Louchev *et al*., 2007; Louchev *et al*., 2008). In particular, section 2 focuses on optical model which integrates 8-level rate dynamics model with the oscillator energy equation. In section 3 we discuss the possibility of G-pulse optimization by doping concentration and by Q-switching control. Section 4 focuses on coupling optical and rate dynamics model with the heat transfer computations. In section 5 we demonstrate main effects in water cooled laser operation. In section 6 we compare main results with available experimental data. In section 7 we outline main conclusions.

2. Pulse generation model

Our study is based on 8-level (see Fig. 1 for excited level scheme) rate dynamics model (Barnes et al. 1996; Walsh *et al*., 2004) describing the population dynamics in Tm,Ho lasers by the following set of equations:

Source: Advances in Solid-State Lasers: Development and Applications, Book edited by: Mikhail Grishin,
ISBN 978-953-7619-80-0, pp. 630, February 2010, INTECH, Croatia, downloaded from SCIYO.COM

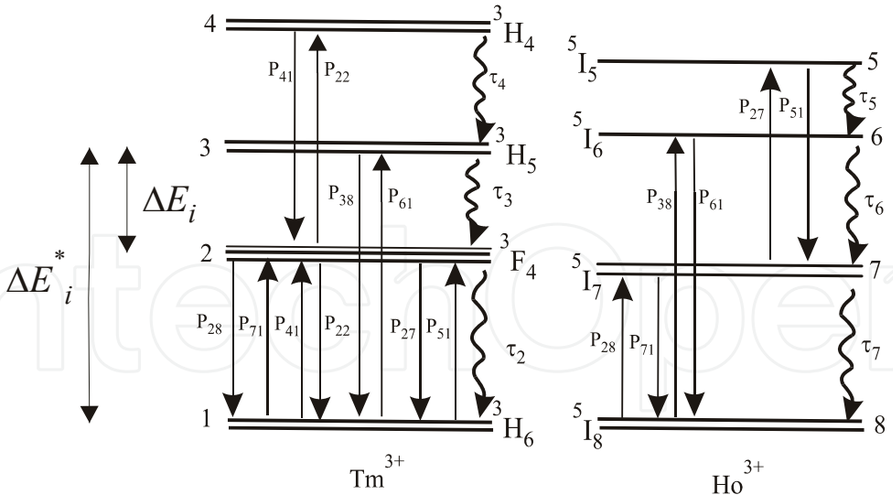

Fig. 1. Energy transfer processes in Tm, Ho doped materials.

$$\frac{dn_1}{dt} = -R_p(t,z,r) + \frac{n_2}{\tau_2} + p_{28}n_2n_8 - p_{71}n_7n_1 - p_{41}n_4n_1 + p_{22}n_2^2, \quad (1)$$
$$+ p_{27}n_2n_7 - p_{51}n_5n_1 - p_{61}n_6n_1 + p_{38}n_3n_8$$

$$\frac{dn_2}{dt} = -\frac{n_2}{\tau_2} + \frac{n_3}{\tau_3} - p_{28}n_2n_8 + p_{71}n_7n_1 + 2p_{41}n_4n_1 - 2p_{22}n_2^2, \quad (2)$$
$$- p_{27}n_2n_7 + p_{51}n_5n_1$$

$$\frac{dn_3}{dt} = -\frac{n_3}{\tau_3} + \frac{n_4}{\tau_4} + p_{61}n_6n_1 - p_{38}n_3n_8, \quad (3)$$

$$\frac{dn_4}{dt} = R_p(t,z,r) - \frac{n_4}{\tau_4} - p_{41}n_4n_1 + p_{22}n_2^2, \quad (4)$$

$$\frac{dn_5}{dt} = -\frac{n_5}{\tau_5} + p_{27}n_7n_2 - p_{51}n_5n_1, \quad (5)$$

$$\frac{dn_6}{dt} = -\frac{n_6}{\tau_6} + \frac{n_5}{\tau_5} - p_{61}n_6n_1 + p_{38}n_8n_3, \quad (6)$$

For the upper laser state ($^5I_7$):

$$\frac{dn_7}{dt} = -\frac{n_7}{\tau_7} + \frac{n_6}{\tau_6} + p_{28}n_2n_8 - p_{71}n_7n_1 - p_{27}n_2n_7 + p_{51}n_5n_1 - \frac{c\sigma_{se}}{\eta}(f_7n_7 - f_8n_8)\varphi(t,\mathbf{r}), \quad (7)$$

For the lower laser state ($^5I_8$):

$$\frac{dn_8}{dt} = \frac{n_7}{\tau_7} - p_{28}n_2n_8 + p_{71}n_7n_1 + p_{61}n_6n_1 - p_{38}n_3n_8 + \frac{c\sigma_{se}}{\eta}(f_7n_7 - f_8n_8)\varphi(t,\mathbf{r}), \quad (8)$$

where n_i are the state concentrations, p_{ij} are the probabilities of the optical transitions (Walsh *et al.*, 2004), η is the refractive index, τ_i are the state lifetimes, $R_p(t,z,r)$ is the pumping source space and time distribution, σ_{se} is the stimulated emission cross-section, f_i are the Boltzmann populations factors and $\phi(t,\mathbf{r})$ is the local laser photon density with dimensionality of $1/m^3$.

The local laser photon density is represented via the product of (i) the total number of photons depending on t and (ii) the normalized space distribution function as $\phi(t,\mathbf{r}) = \Phi_0(t)\phi_0(r,z)$. The resulting equation for total photon number, $\Phi_0(t)$, inside the oscillator cavity is given by the differential equation (Risk, 1988; Rustad & Stenersen, 1996; Walsh *et al.*, 2004; Černý & Burns, 2005):

$$\frac{d\Phi_0(t)}{dt} = \frac{\Phi_0(t)c\sigma_{se}}{\eta}\iiint_{V_{cr}}(f_7 n_7 - f_8 n_8)\phi_0(r,z)dV - \frac{\Phi_0(t)}{\tau_c} + \frac{\varepsilon}{\tau_7}\iiint_{V_{cr}} n_7 dV\,, \tag{9}$$

which includes the integrals of the stimulated and spontaneous emissions over the crystal volume, V_{cr}, and where τ_c is the cavity time, and $\varepsilon \approx 10^{-7}$-$10^{-8}$ is the coefficient which takes into account the proportion of photons spontaneously emitted within the solid angle of resonator mirrors, thereby initiating the development of the laser beam.

For the operating resonator the cavity time is:

$$\tau_c^{-1} = \frac{c}{2L_{opt}}\left[-\ln R_1 - \ln(1-T_{out}) + \beta + 2\sum_i \alpha_i l_i\right], \tag{10}$$

where $L_{opt} = L_{cav} + (\eta - 1)L_{cr}$ is the characteristic optical length, L_{cav} is the cavity length and L_{cr} is the crystal length; R_l is the back mirror reflectance, T_{out} is the output mirror transmittance and β is the parameter used in our simulations for the optical loss associated with the active Q-switching: β=0 for the open resonator and $\beta >> -\ln R_1 - \ln(1-T_{out})$ for the closed resonator.

The value of $2\sum_i \alpha_i l_i$ in Eq. (10) represents the sum of absorption losses in different elements along which laser beam propagates inside the cavity. This value should be small to ensure the feasibility of the laser operation. Otherwise the significant part of the laser energy generated by the crystal is lost.

For the case of ≈500 ns pulse generation the cavity length L_{cav} >> L_{cr} and the laser beam radius inside the crystal may be considered to be constant. The spatial distribution of photons inside the operating crystal is simplified as:

$$\phi_0(r,z) = \frac{2}{\pi w_0^2 L_{cav}}\exp\left(\frac{-2r^2}{w_0^2}\right), \tag{11}$$

where w_0 is the beam waist size of TEM_{00} mode defined by the resonator parameters (for instance, for the simplest case of the confocal spherical resonator one has $w_0 = \sqrt{L_{cav}\lambda_l/2\pi}$).

The solution of the rates equation together with main oscillator equation gives the value of the output power, (W), as:

$$J(t) = \Phi_0(t)\frac{ch\nu_{las}}{2L_{opt}}\ln\frac{1}{1-T_{out}}, \tag{12}$$

We consider Tm,Ho:YLF operation side pumped by 780 nm LD radiation. For 6 % Tm doped YLF one finds for the absorption coefficient $\alpha=\sigma_a N_{Tm}\approx 2.8$ cm^{-1}. Thus, a 2 mm diameter YLF crystal is able to absorb $(1-\exp(-2\alpha d))\approx 0.67$-fraction of the incident beam flux in the case of the double-pass pumping scheme providing high uniformity of the absorbed flux over the crystal volume. High incident fluxes are able, in fact, to deplete the $^3H_6$-level in Tm^{3+} and to inhibit absorption (Rustad & Stenersen, 1996; Černý & Burns, 2005). However, when the concentration of the $^3H_6$-level does not fall below 0.9 of the initial Tm-concentration, the related variations of absorption coefficient do not exceed 5 %, and in making simulation one can use for R_p:

$$R_p(t) \approx \frac{\eta_p \eta_a Q_p}{\pi d^2 L_{cr} h \nu_p \Delta t_p}, \tag{13}$$

where $\eta_a = (1-\rho)\left[1-\exp(-2\alpha d)\right]$ is the absorption efficiency of the pumping radiation, ρ is the reflection factor of pumping radiation, Q_p is the pumping pulse energy, Δt_p is the pumping pulse duration, $\eta_p\approx 1.3$ is the pumping quantum efficiency for Tm,Ho:YLF.

3. Giant pulse optimization

Model parameters used for Tm,Ho:YLF in the simulations are fully specified by Walsh *et al*. (2004). Other parameters used in the simulations reported below are: crystal length L_{cr}=2 cm, crystal diameter d=2 mm, cavity length L_{cav}=1 m, output transmittance T=0.05, reflectance R_1=0.98, and beam waist radius w_0=0.85 mm. The simulations reveal two main effects important for efficiency optimization for producing nanosecond G-pulses.

Fig. 2 shows a simulation results for 6 % Tm doping and two values of Ho doping, 0.4 and 1.0 %, for the case of normal pulse operation (without Q-switch) demonstrating a series of relaxation oscillations. The pumping (780 nm laser diode) time for both modes is 0.5 ms and the total absorbed energy $\eta_a Q_p$ =1.8 J. Fig.2 (a) shows the power oscillations for the cases of Ho = 0.4 and 1.0 % respectively, whereas Fig. 2 (b) shows the output pulse energies versus time. The final pulse energy for the 0.4 % Ho case (≈0.9 J), is calculated to be higher than that of 1.0 % Ho case (≈0.8 J). However, Fig. 2 (a) shows that the power of the first relaxation spike is higher for the case of 1.0 % Ho. Thus in G-pulse generation the 1.0 % Ho case is able to yield a higher output energy per pulse as compared with the 0.4 % Ho case.

Fig. 3 shows calculations of (a) G-pulse powers and (b) energies versus time for 0.4 % and 1.0 % Ho cases. The calculations assume that Q-switch operation is open by the end of the 0.5 ms pumping period. This figure shows that 1.0 % Ho doping can provide higher energy output per pulse as compared with 0.4 % Ho doping due to significantly larger level of the inverted population achieved after the pumping (See. Fig. 4).

Fig. 5 compares the resulting pulse energy for the normal pulse and for the G-pulse as a function of Ho-concentration for the given 6 % Tm doping. These figures confirm that for the normal pulse 0.4 % Ho doping provides the highest output energy whereas for G-pulse 1.0-1.2 % looks to be optimal.

Let us now focus on the time optimization of G-pulse operation. The above results on G-pulse generation assumed 0.5 ms pumping followed by immediate Q-switch opening. However, Fig. 4 suggests that such Q-switch opening is premature because the inverted population density does not achieve its maximum at the end of pumping.

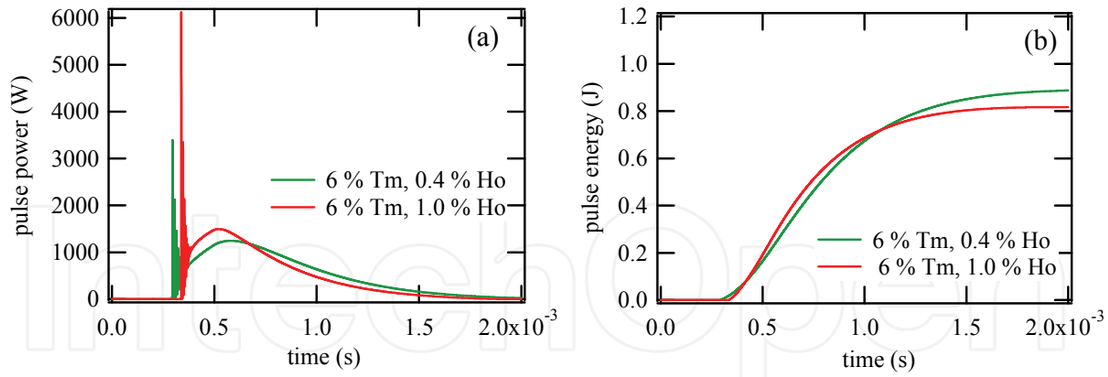

Fig. 2. Pulse generation in normal mode: (a) pulse power versus time and (b) pulse energy versus time for two Tm, Ho concentrations.

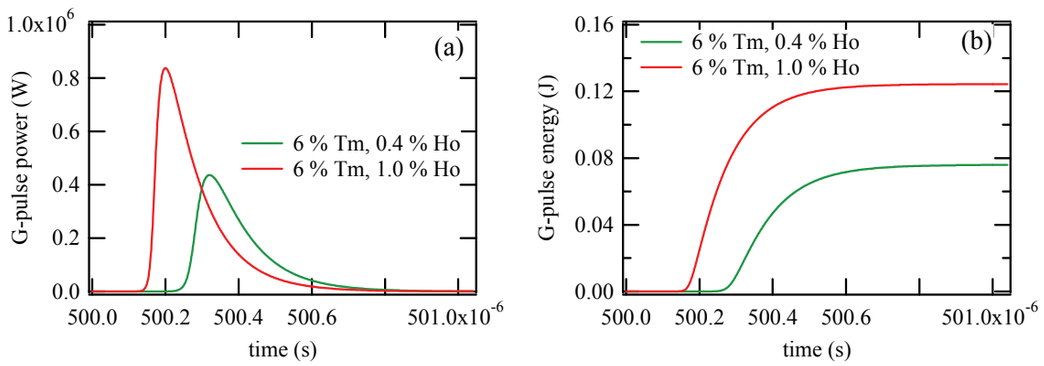

Fig. 3. G-pulse generation: (a) pulse power versus time and (b) pulse energy versus time.

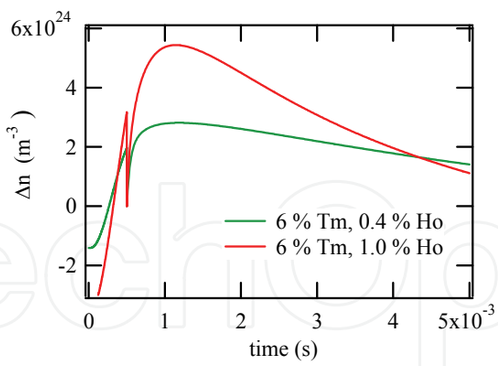

Fig. 4. Inversion population dynamics in G-pulse generation mode.

Now we provide more details to emphasize the importance of proper time control. In particular, Fig. 6 (a) shows the dependence of G-pulse power as function of the time for three characteristic cases: (i) 0.5 ms pumping followed by Q-switch opening (green), giving a pulse energy of ≈0.08 J, (ii) 1.9 ms pumping followed by Q-switch opening (blue) giving a pulse energy of ≈0.11 J and (iii) 0.5 ms pumping followed by Q-switch opening at 1.2 ms (red) giving a pulse energy of ≈0.12 J. Fig. 6 (b) shows the behavior of the inversion population, $\Delta n = f_7 n_7 - f_8 n_8$, for all three cases considered and provides the background

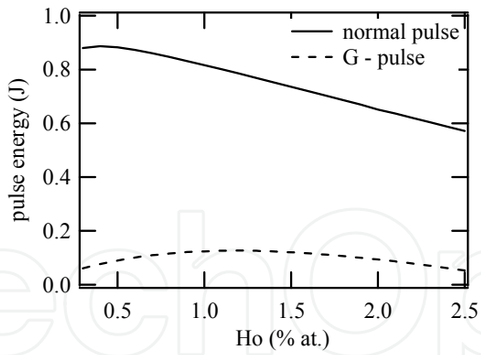

Fig. 5. Comparison of output pulse energy in normal (solid) and G-pulse (dashed) mode.

information for understanding time optimization issues. That is, in the first case the Q-switch is open prior to the moment when maximal population inversion in the Ho^{3+} is achieved and the resulting output G-pulse energy is small. After the pulse is finished and the Q-switch is closed, the excited Tm^{3+} state $^3F_4$ continues to transfer excitation towards the Ho^{3+} $^5I_8$. In this case a very significant part of the excitation "stored" initially in Tm^{3+} is transferred to Ho^{3+} after the G-pulse generation, and later on uselessly dissipated through spontaneous radiation and non-radiative transitions. In the second case of the significantly increased pumping time 1.9 ms with simultaneous opening of Q-switch a significantly higher generated pulse energy is achieved, due to significantly higher electronic excitation energy stored on the Ho^{3+} $^5I_7$ state by the end of the pumping pulse. The third case corresponds to the situation when a relatively short pumping time of 0.5 ms is used together with 0.7 ms delay in opening the Q-switch. This case gives maximal energy output of ≈0.12 J in G-pulse generation because the Q-switch opens exactly at the moment when the concentration on the lasing Ho^{3+} $^5I_7$ state and the value of Δn reach their maximum, allowing maximal energy extraction by the laser pulse.

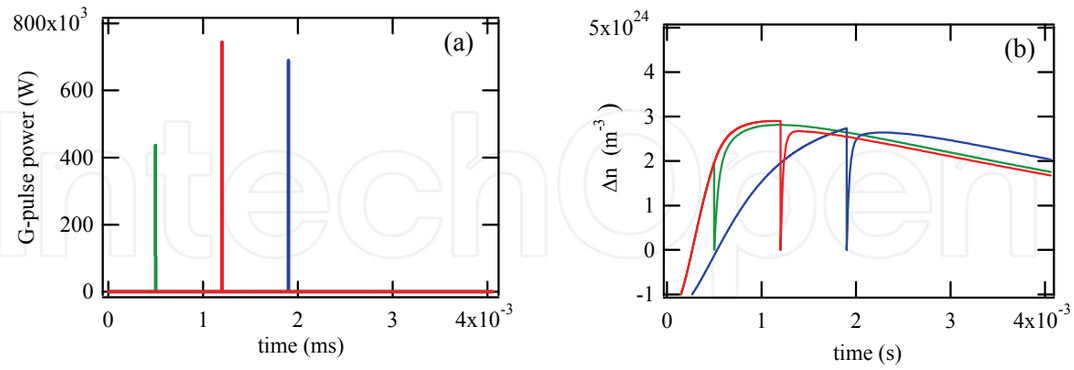

Fig. 6. Optimization of G-pulse generation: (a) G-pulse powers versus time and (b) corresponding population inversion densities versus time for three different scenarios.

Fig. 7 shows final results on G-pulse energy optimization: (a) for the case of extended LD pumping within the range 0.5 - 10 ms followed by immediate Q-switch opening and (b) 0.5 ms LD pumping with delayed Q-switch opening. Energy maxima exist in both cases: at ≈1.9 ms for (a) and at ≈1.2 ms for (b). However, case (b) provides the higher absolute maximum.

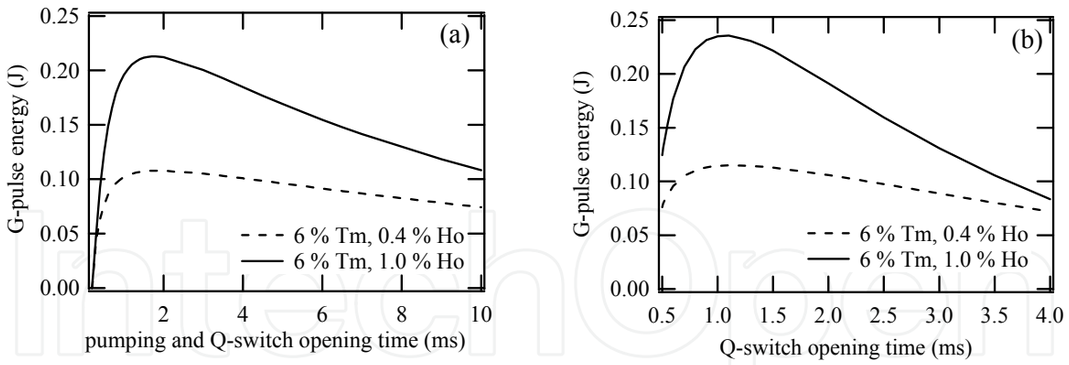

Fig. 7. Optimization of operation times: (a) Q-switch is open by the end of pumping and (b) pumping time is 0.5 ms and Q-switch is open after a delay.

It is worth noting that the delay between the pumping period and Q-switch opening shown above to optimize the energy pulse is associated with the characteristic time of the electronic transfer from the upper exited state $^3H_4$ to $^3F_4$ and, later on, towards $^5I_7$. Our simulation based on the above model shows that the excitation transfer from the $^3F_4$ state towards the $^5I_7$ state happens without any significant deceleration whereas significant delay is associated with the $^3H_4 \rightarrow {}^3F_4$ radiation transfer process, i.e. the rise in concentration at the Tm3+ $^3H_4$ state, defined by the pumping period used, and the depletion of this level, defined by the two-photon process $p_{41}n_4n_1$ and requiring ≈0.7 ms. In the case of extended pumping of several ms this delay does not play a very significant role, in contrast with short pumping times. The decrease in the delivered G-pulse energy shown in both cases for long times is associated with the increasing role of spontaneous radiation loss from both $^3F_4$ and $^5I_7$ states which have characteristic lifetimes of 16 and 15 ms respectively.

To finalize the discussion we would like to note that a ≈0.7 ms delay between pumping and achieving the maximal population inversion density in a Tm,Ho:YLF laser found in this study is experimentally supported by the observation of the amplification signal in a Tm,Ho:YLF crystal pumped by a 780 nm radiation pulse of 65 μs duration (Bruneau *et al.*, 1998). Data recorded for the YLF case shows the amplification signal maximum at 0.6-0.7 ms after the start of the pumping. However, the data for Tm,Ho:YAG operation does not show any significant delay between pumping period and maximal amplification signal.

4. Thermal model

The heat absorbed inside the crystal leads to a temperature increase over the crystal volume. For high power operation this temperature shift is able to change the local values of the Boltzmann population factors of the upper and lower lasing levels:

$$f_i(t,\mathbf{r}) = \frac{g_i \exp\left[-E_i/k_B T(t,\mathbf{r})\right]}{\sum_j g_j \exp\left[-E_j/k_B T(t,\mathbf{r})\right]}, \tag{14}$$

where k_B is the Boltzmann constant, g_i is the degeneracy of the *i*-level, and $T(t,\mathbf{r})$ is the local temperature.

Generally, the crystal is heated via lattice vibrations due to non-radiative decay of electrons from all levels involved in the excitations. The local heat source is defined by:

$$q_{cr}(t,\mathbf{r}) = \sum_{i=2}^{7} \Delta E_i \, n_i / \tau_{inr} \,, \tag{15}$$

where ΔE_i is the energy difference between the *i*-manifold and the next lower manifold into which the electron makes the transition (Fig. 1) and τ_{inr} are the non-radiative times inversely proportional to the non-radiative transition probabilities.

In order to avoid difficulties in defining the probabilities of non-radiative transitions, an estimate of the heat source can be made via the difference between the pumped energy and the energy of stimulated and spontaneous radiation leaving the crystal (Bruneau *et al*, 1998). This approach is mainly used for the CW mode or as an averaged estimate for high-repetition pulsed mode. However, we (Louchev et al., 2008) use this approach for normal or Q-switched mode operation by introducing a modification which takes into account the rate, $\sum_{i=2}^{7} \Delta E_i^* dn_i / dt$, at which the pumped energy is stored inside Tm^{3+} and Ho^{3+} ions as:

$$q_{cr}(t,\mathbf{r}) = R_p(t) h\nu_p - c\sigma_{se}\eta^{-1} h\nu_l (f_7 n_7 - f_8 n_8)\phi(t,\mathbf{r}) - \sum_{i=2}^{7} \Delta E_i \, n_i / \tau_{ir} - \sum_{i=2}^{7} \Delta E_i^* dn_i / dt \,, \tag{16}$$

where in addition to ΔE_i we introduce the energy difference between the *i*-manifold and the ground state ΔE_i^* (Fig. 1), ν_p is the pumping radiation frequency, ν_l is the lasing frequency and τ_{ir} are the corresponding radiative times (Walsh *et al*., 2004).

The calculation of Eq. (16) for the Tm,Ho:YLF laser reveals several effects significant for energy extraction by lasing pulse. First, Fig. 8 shows (a) G-pulse power and (b) the energy and (c) optical loss balance integrated over the crystal volume versus time. In fact, Fig. 8 (b) reveals a very significant extension of the heat release period as compared with the pumping period. In particular, it shows that the heat is released inside the crystal over a period of ≈10 ms, whereas the pumping period is 0.5 ms during which only ≈30 % of heat is released. A two-time lower resulting temperature increase is achieved in crystal prior to G-pulse generation (1.2 ms) as follows from an estimate neglecting the thermal conductivity effect:

$$\Delta T_{cr}(t,\mathbf{r}) \approx \frac{1}{\rho c} \int_0^t q_{cr}(t,\mathbf{r}) dt \,. \tag{17}$$

Second, Fig. 8 (b) also shows that in the final energy balance ≈0.12 J corresponds to the G-pulse energy, ≈0.75 J corresponds to the heat released inside the crystal and ≈0.84 J corresponds to the energy lost by spontaneous emission. Thus, about 43 % of the pumped energy is directly converted into heat. We should note that the estimates of heat release based on 2-level rate equations treat this value as the difference between the pumped energy and the optical energy of the laser pulse and the spontaneous emission from two levels, $^3F_4$ and $^5I_7$ (Bruneau *et al*, 1998). The energy spontaneously emitted by other levels, i.e. $^3H_5$, $^3H_4$, $^5I_5$ and $^5I_6$, are implicitly included into the heat released inside the crystal (Bruneau *et al*, 1998). The 8-level model used here shows that the contribution of the $^5I_5$ and $^5I_6$ levels into the spontaneous emission loss is negligibly small, whereas the contribution of $^3H_4$ and $^3H_5$ appears to be quite significant, ≈0.1 and ≈0.4 J, respectively. Adding these

values to the heat release of ≈0.75 J gives ≈70 %, similar to the result from the 2-level model (Bruneau *et al*, 1998).

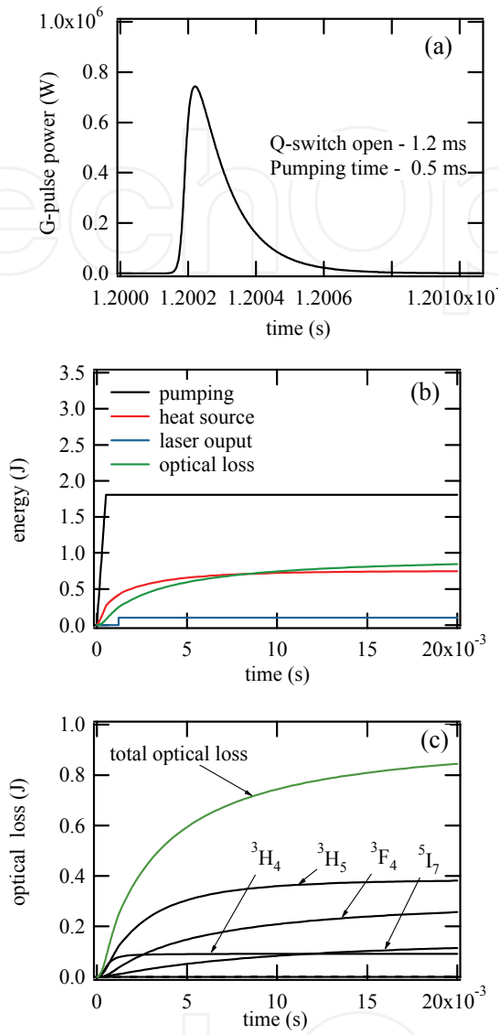

Fig. 8. Pulse power, energy balance versus time during laser operation: (a) G-pulse power with corresponding (b) energy balance and (c) optical loss by spontaneous radiation from different levels.

Thus, only ≈43 % of the pumped energy is released directly as heat inside the crystal, whereas ≈45 % is spontaneously emitted radiation from the crystal at wavelengths: λ_2=1.93 μm, λ_3=4.32 μm, λ_4=2.46 μm and λ_7=2.07 μm. These wavelengths are within the transparency range of the crystal and are therefore able to leave the crystal. Fig. 8 (c) shows the values of the total optical loss, $\sum_{i=2}^{7} \Delta E_i \, n_i / \tau_{ir}$, and also the losses emitted from all levels, $\Delta E_i \, n_i / \tau_{ir}$ integrated over the crystal volume. These radiation fluxes leaving the crystal are absorbed by the water flow typically used for crystal cooling. The water absorption coefficients for these wavelengths are given by Wieliczka *et al.*, 1989: α_2=124 cm^{-1}, α_3=300 cm^{-1},

α_4=63.5 cm^{-1} and α_7=31 cm^{-1}. That is, the spontaneously emitted fluxes leaving the crystal are absorbed within lengths of $\approx \alpha_i^{-1}$, i.e. within 80, 33, 157 and 320 μm from the surface, respectively. The absorption of these fluxes in the vicinity of the crystal surface can significantly inhibit heat dissipation from the crystal. The heat transfer to the water flow depends on the Reynolds number, *Re*, defining the level of the flow turbulency dependent on the water flow rate through the channel inside which the operating crystal is set up. Numerical estimates show that for the typical coaxial crystal in a tube water channel geometry and typical flow rates, the value of the heat transfer coefficient is h=10^3-10^5 W/m^2 K (Koechner, 2006). The main thermal resistance to the heat flow from the crystal surface is due to the thermal boundary layer, δ_T, within which the heat conductance dominates over the convective transport. The estimate of δ_T follows from the equivalency of heat fluxes at crystal-water syrface:

$$-k_{cr}\partial T_{cr}/\partial r\big|_{sur} = -k_w \partial T_w/\partial r\big|_{sur} = h(T_{cr}\big|_{sur} - T_{w\infty}),$$

where k_{cr}≈6 and k_w≈0.6 W/m K are the thermal conductivity of crystal and water, respectively. That is, using $\partial T_w/\partial r\big|_{sur} \approx -(T_{cr}\big|_{sur} - T_{w\infty})/\delta_T$ one finally obtains for h=10^3-10^5 W/m^2 K:

$$\delta_T \approx k_w / h \approx \text{6-600 μm.} \tag{18}$$

Thus, the spontaneous IR fluxes are absorbed by water within a distance where the heat transfer is dominated by the thermal conductivity. Hence, the absorption of these fluxes is able to significantly inhibit the heat dissipation from the crystal. In order to consider the thermal effect we simulate the complex heat transfer non-steady state, two-dimensional problem by coupling the above optical model with the heat generation and heat transport through the operating crystal, and the water boundary layer inside which the absorption of spontaneously emitted IR radiation takes place. The radially symmetric temperature distribution inside the cylindrical crystal, $T_{cr}(t,\mathbf{r})$, and the thermal boundary layer in water, $T_w(t,\mathbf{r})$, are defined by:

$$\rho_i C_i \,\partial T_i/\partial t = \mathrm{div}(k_i \mathrm{grad} T_i) + q_i(t,\mathrm{r}), \tag{19}$$

for crystal (i=*cr*) and water (i=*w*) with the boundary condition $T_w = T_{w\infty}$ at $r = R_0 + \delta_T$, where $\delta_T = R_0\left[\exp\left(k_w/R_0 h\right) - 1\right]$ takes into account the radial curvature.
Heat source density inside the crystal is defined by Eq. (16) whereas the heat source density due to the absorption of spontaneously emitted IR fluxes in water is defined by:

$$q_w(t,r) = \frac{R_0}{r}\sum_i J_{0i}(t)\alpha_i \exp\left[-\alpha_i (r - R_0)\right], \tag{20}$$

where $J_{0i}(t)$ are the IR flux densities isotropically leaving the crystal given by:

$$J_{0i}(t) = \frac{1}{S_{cr}}\int_V \Delta E_i n_i(t,\mathrm{r})/\tau_{ir} dV \cdot \tag{21}$$

The effect of IR radiation absorption is negligibly small for h>10^5 W/m^2 K, when $\delta_T << \alpha_i^{-1}$. However, for h≈10^4 W/m^2 K (δ_T ≈60 μm) this effect is very significant, and can lead to the onset of an inverted temperature distribution inside the crystal when the temperature inside the boundary layer is higher than that inside the crystal.

5. Coupled thermo-optical modeling

In this section we consider coupled optical and thermal model results obtained for G-pulse generation by a Tm,Ho:YLF laser aimed to produce ≈0.1 J pulses of 100-500 ns duration. In particular, we simulate here 20-50 Hz active Q-switched laser operation side-pumped by 0.5 ms LD pulses of ≈785 nm wavelength. In Fig. 9 we show G-pulse simulation results for a 2 cm long 2 mm diameter crystal placed inside a 1 m long cavity with a 0.85 mm radius waist. The Q-switch is opened after a 0.5 ms pumping period with a delay of 1.2 ms to ensure that the G-pulse generation starts after the maximal possible gain is achieved.
In particular, in Fig. 9 we show the results of G-pulse stabilization for h=104 W/m^2 K for three different cases: (a) 2 mm diameter crystal with L_{cr}=2 cm, pumping energy 1.8 J and f=20 Hz operation, (b) 4 mm diameter crystal with L_{cr}=2 cm, pumping energy 4.0 J and f =20 Hz operation, and (c) 4 mm diameter crystal with L_{cr}=2 cm, pumping energy 4.0 J, and f =50 Hz operation.

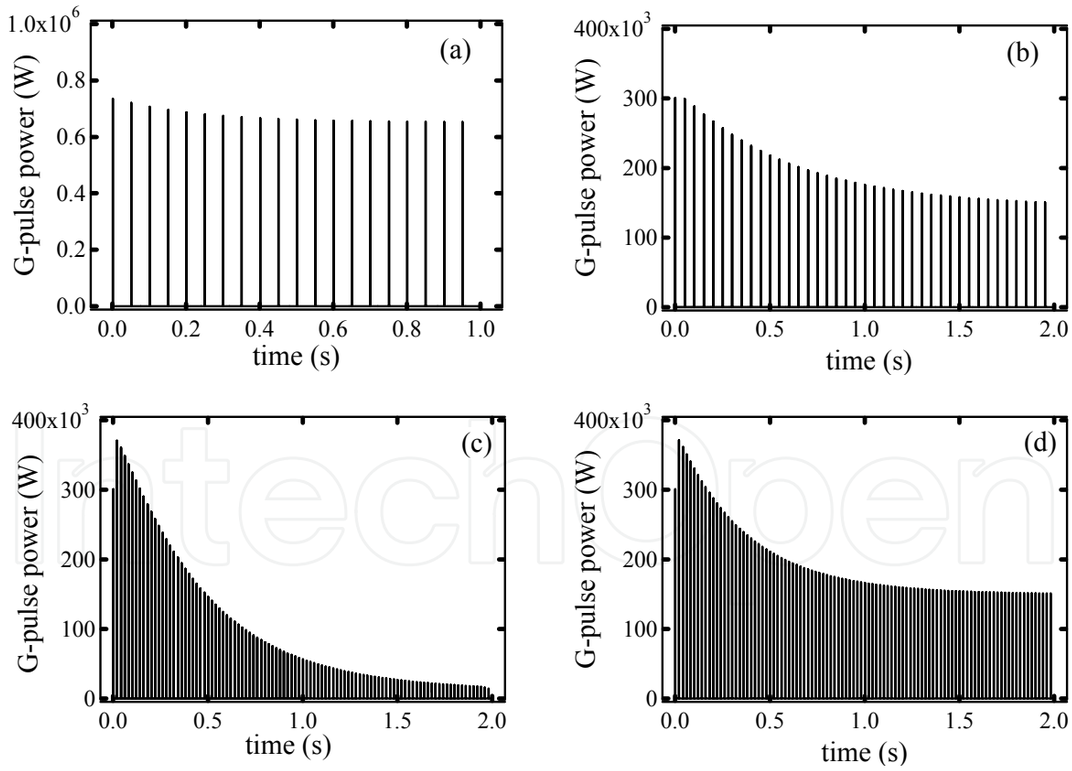

Fig. 9. G-pulse power stabilization versus time for (a) 2 mm diameter crystal, 1.8 J pumping, f=20 Hz and h=10^4 W/m^2 K, (b) 4 mm diameter crystal, 4.0 J pumping, f=20 Hz and h=10^4 W/m^2 K, (c) 4 mm diameter crystal, 4.0 J pumping, f=50 Hz and h=10^4 W/m^2 K and (d) 4 mm diameter crystal, 4.0 J pumping, f=50 Hz and h=10^5 W/m^2 K.

Additionally in Fig.9 (d) we show the pulse power for the case of enhanced heat transfer with h=10^5 W/m^2 K for 4 mm diameter crystal with L_{cr}=2 cm, pumping energy 4.0 J and f =50 Hz operation. In this case the spontaneous radiation leaving the crystal is absorbed outside of the boundary layer, $\delta_T \approx k_w / h \approx 6$ μm.

The case (a) corresponds to ≈0.12 J pulse generation. In 20 Hz repetition rate operation the initial pulse power for this case is decreased by ≈11 %. The case (b) corresponds to ≈0.13 J pulse generation. In this case, after stabilization in 20 Hz repetition rate operation the G-pulse looses about 40 % of its power and energy. In case (c) for 50 Hz repetition rate operation the G-pulse looses about 95 % of its initial power. In case (d) when heat transfer is enhanced the pulse energy decrease is about 60 %. One peculiar point worth noting here is that in 50 Hz operation the second pulse has a 20 % higher pulse energy than the first pulse (see Fig. 9 (c) and (d)). This is due to the inversion population remaining after the first pulse during 20 ms and summarized with the effect of the second pumping pulse.

The temperature evolution and stabilization related to these cases are shown in Fig. 10 (a-d) where the temperature is shown at the crystal axis and surface. The maximal temperatures are achieved at the end of ≈5 ms period and not at the end of pumping period. In particular, Fig. 10 (a), (b) and (c) show that at the initial stage the temperature at the crystal surface is higher than that at the crystal axis. This is due to the high optical fluxes spontaneously emitted from the crystal and heating water near the crystal surface. However, with time and operation stabilization the temperature inside the crystal becomes higher than that at the surface, and the heat from inside the crystal dissipates to the water. In the case (d) the temperature at the surface does not exceed that at the crystal axis even in the initial stage because for this case the spontaneous radiation is absorbed outside of the boundary layer ($\delta_T \approx 6$ μm< <α^{-1}).

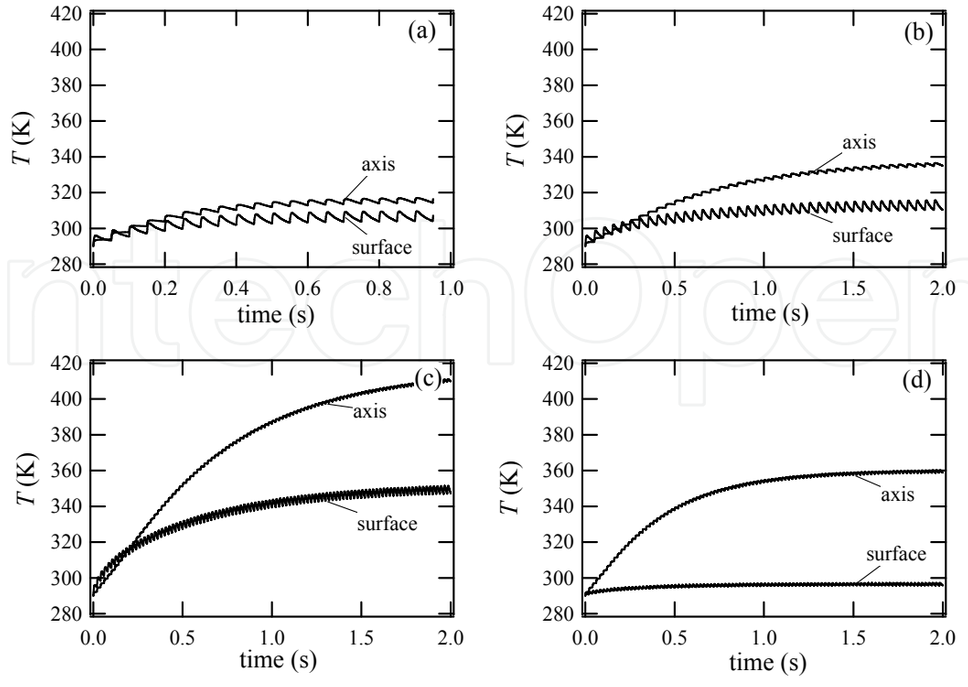

Fig. 10. Temperature evolution at crystal axis and surface for the cases defined in Fig. 9.

Fig. 11 shows the temperature distributions versus radius for the case of 4 J pumping of the crystal 4 mm in diameter and L_{cr}=20 mm for f=20 Hz operation and h=10^4 W/m^2 K. The temperature distribution are given (a) for the first pulse and (b) after pulse energy and temperature stabilization is achieved. The temperature distributions are given immediately after the pumping, 1.2 ms, (solid) and after the full pulse period of 50 ms (dashed). Fig. 11 (a) shows that for the first pulse the temperature in the boundary layer is higher than that in crystal due to the effect of absorption of IR radiation inside the boundary layer. However, after the pulse energy and temperature stabilization shown in Fig. 11 (b) this effect does not look very strong. However, in fact, this effect averaged over the pulse period remains to be very significant in resulting temperature field. After the stabilization, the temperature amplitude inside the crystal over one period decreases to the level of ≈1 K.

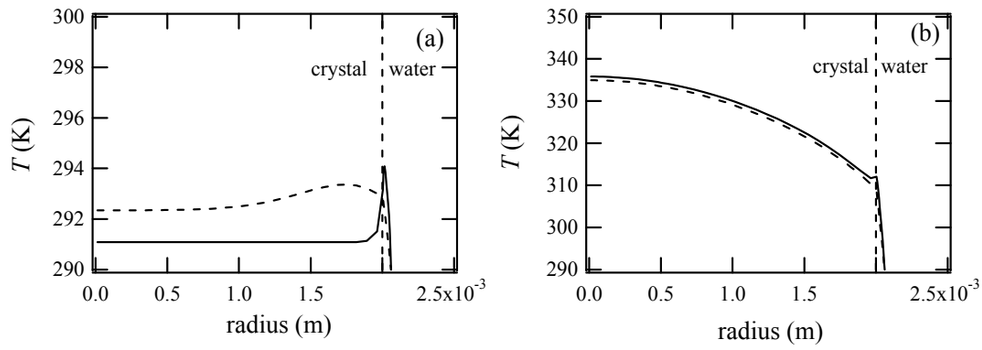

Fig. 11. Temperature distributions versus radius for 1.2 ms (solid) and 50 ms (dashed) for f=20 Hz operation: (a) the first pulse and (b) after pulse energy stabilization.

Let us discuss the above obtained simulation results within the framework of simplistic estimates. First, the effect of heat dissipation inhibition due to the radiation fluxes absorbed within the boundary layer shown by the above simulation can be demonstrated by an analytically resolvable model using the plane steady-state boundary layer approximation ($\delta_T << R_0$):

$$k_w d^2T_w / dr^2 + \sum_i \bar{J}_{0i}\,\alpha_i \exp(-\alpha_i r) = 0\,, \tag{22}$$

with the mean radiation fluxes leaving the crystal surface given by :

$$\bar{J}_{0i} = \frac{\nu_p}{S_{cr}} \int_t dt \int_V \Delta E_i n_i / \tau_{ir} dV\,, \tag{23}$$

where V_{cr}=$\pi R_0^2 L_{cr}$ is the crystal volume, S_{cr}≈$2\pi R_0 L_{cr}$ is the crystal surface through which the spontaneous radiation leaves the crystal and the boundary condition is written at r=0 as $T_w = T_s$ and at r=$\delta_T = k_w / h$ as $T_w = T_w^*$.

After resolving this simplified model one can obtain the following analytical expression for the modified heat transfer coefficient:

$$h^* = -\frac{k_w}{T_s - T_w}\left.\frac{\partial T_w}{\partial r}\right|_{r=R_0} = h - \frac{1}{T_s - T_w}\sum_i J_{oi}\left\{1 - \frac{h}{\alpha_i k_w}\left[1 - \exp\left(-\frac{\alpha_i k_w}{h}\right)\right]\right\}, \tag{24}$$

which takes into account the effect of spontaneous radiation absorbed within the thermal boundary layer on the heat transfer to the water.

One can see that this estimate gives automatically $h^* = h$ for the case when absorption does not take place within the boundary layer, or primarily occurs outside it. The estimate for the value of h^*/h defined by Eq. (24) is shown in Fig. 12 for the possible range of h=10^3-10^5 W/m^2 K and for IR fluxes corresponding to the simulations given in Fig.9 (a) and averaged over the characteristic time of $\Delta t = \nu^{-1}$ =50 ms. In particular, Fig. 12 shows that even for this simplified treatment this effect appears to be very significant. That is, for low values of h<10^4 W/m^2 K the effective heat transfer coefficient falls rapidly and for h=10^3 W/m^2 K the value of h^* tends to zero. Eq. (24) also shows that h^* can become negative (for low h values or high radiation fluxes) meaning that the water layer near the crystal surface can have a temperature that exceeds that of the crystal surface (as shown in simulation on Fig. 11). For a typical value of h=10^4 W/m^2 K (δ_T≈60 μm) Eq. (24) gives h^*≈ 0.55 h whereas for h=10^5 W/m^2 K (δ_T≈6 μm) the effect decreases giving h^*≈ 0.94 h. The effect of radiation absorption in water becomes negligibly small for high values of h>10^5 W/m^2 K, i.e. when the thickness of the boundary layer becomes smaller than a typical absorption length and all radiation is absorbed outside of the boundary layer.

Second, we have to note here that after onset of operation stabilization the mean temperature distribution across the crystal radius (averaged over one period) is well approximated by modified analytical quasi-steady state approximation (Koechner, 2006):

$$T(r) = T_w^* + \frac{q_{av} R_0}{2h^*} + \frac{q_{av}}{2k_{cr}}\left(R_0^2 - r^2\right), \tag{25}$$

where for q_{av} we use the averaged heat source density defined by the integral over the characteristic pulse period, $\Delta t = \nu^{-1}$, and the crystal volume as:

$$q_{av} = \frac{1}{V_{cr}\Delta t}\int_{\Delta t}\int_{V_{cr}} q_{cr}(\mathbf{r},t)\,dt\,dV\,. \tag{26}$$

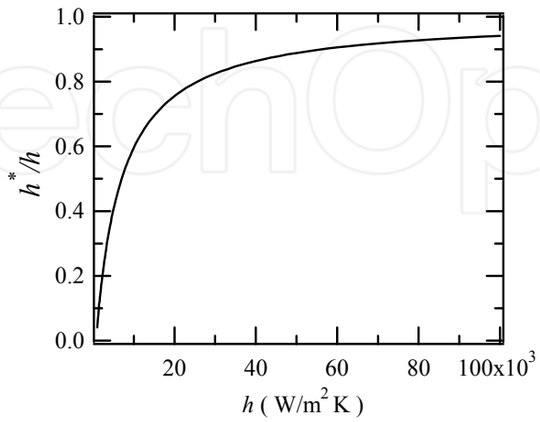

Fig. 12. The influence of absorbed infrared radiation spontaneously emitted from Tm-Ho laser on the heat transfer coefficient from the surface of the operating crystal to the water for 2 mm diameter crystal, 1.8 J pumping and f=20 Hz.

Equation (25) explains well our simulation results given in Fig.9 (c) and (d), and Fig. 10 (c) and (d) which show that the absolute temperature level achieved during laser operation can be decreased by more intensive heat removal (by using higher water flow) or by using lower temperature water (in our simulations T_w^*=290 K). In effect, Eq. (25) shows that intensification of the heat transfer, i.e. increase in h^*, allows one to decrease the temperature of the crystal surface to that of water T_w^* (making $q_{av}R_0/2h^* \to 0$). However, the temperature difference installed across the crystal radius remains the same (≈30 K) because it is defined by the value of $q_{av}R_0^2/2k_{cr}$, and depends only on the crystal radius, crystal heat conductance and the heat source density inside the crystal.

High temperature gradient across the crystal radius is known to lead to thermal lensing effects and output laser beam distortions (Akhmanov *et al*.; 1979). Thus, in order to inhibit the temperature gradient across the radius and onset of thermal lenzing one should (i) decrease the pumping energy per crystal volume unit and (ii) to decrease the crystal radius as shown in Figs. 9 (a) and 10 (a) where significantly lower temperature gradient for 2 mm diameter crystal are found as compared with 4 mm crystal diameter cases shown on Figs. 9 and 10 (b) - (d).

Finally, we have to note that Tm,Ho:YAG has lower temperature gradients across the radius due to two factors. First, YAG has larger heat conductance (11 W/m K) as compared with YLF (6 W/mK). Second, Tm.Ho:YAG has 2 times higher Tm $^3H_4$ absorption cross-section (σ_a=7x10^{-21} cm^2) as compared with Tm,Ho:YLF (σ_a =3.4x10^{-21} cm^2) which allows one to use lower crystal radii with the same absorption efficiency. That is, for 6 % Tm doped YLF and YAG one finds α_{YLF}≈2.82 cm^{-1} and α_{YAG}≈5.75 cm^{-1}. Thus, 2 mm diameter crystal is able to absorb (1-exp(-αd))-fraction of the incident beam, i.e. 43 % in case of YLF and 70 % in case of YAG. For double passing scheme 2 mm YAG absorbs 90 % of the side-pumped incident beam whereas YLF absorbs only 68 %. In case of YLF 90% absorption is achieved in crystals of 4 mm in diameter. It should be noted that increase in the crystal radius increases the pumping density and also heat source density. However, 4-times increase in the heat source density in 2mm YAG crystal as compared with 4 mm YLF is exactly compensated by 4-time decrease in the temperature gradient across the radius shown by Eq. (25).

6. Model verification

6.1 Absorption losses

As noted in section 2 the absorption loss $2\sum_i \alpha_i l_i$ (in Eq. (10)) taking place inside the cavity is able to decrease significantly and even completely inhibit laser output. In particular, Fig. 13 shows the typical dependence of G-pulse energy from Tm,Ho:YLF laser versus the absorption loss inside the cavity. The absorption loss can be due to several factors. First, for the case of 2 μm lasers this effect can be due to the water vapor present inside the cavity. In effect, the absorption of water for ≈2.1 μm is α≈31 cm^{-1} (Wieliczka, *et al*., 1989). The absorption coefficient is defined by the absorption cross-section and water molecules density $\alpha = \sigma n$. Thus, the absorption cross-section for water is $\sigma = \alpha / n_w = \alpha\rho_w / m$≈9.3x10^{-22} cm^2 (where n_w is the density of molecules in water, ρ_w is the water density and m is the molecular mass of water). For the room temperature 24^0 C the equilibrium water pressure P≈3x10^3 Pa. Thus, for the humidity 50 % the vapor density is

$n_v=P_v/2k_BT\approx0.36x10^{18}$ cm^{-3}. Respectively, the value of the absorption coefficient is $\alpha=\sigma\ n_v\approx3.3x10^{-4}$ cm^{-1} and for the cavity l=300 cm in length one gets $2\sum_i\alpha_i l_i\approx0.2$, which suggests that the air humidity can completely inhibit laser operation. However, for a short cavity length of 30 cm $2\sum_i\alpha_i l_i\approx0.02$ and G-pulse energy loss is ≈25 %.

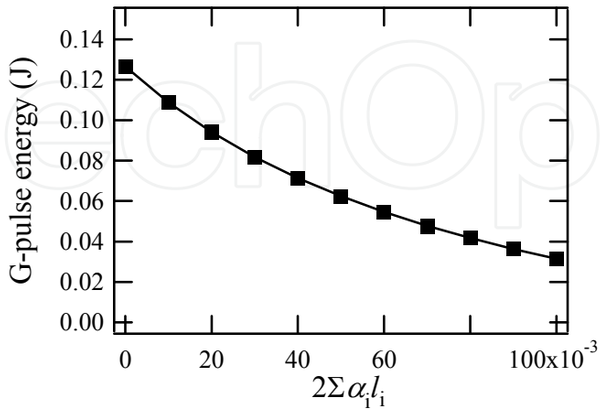

Fig. 13. The effect of absorption loss inside the cavity.

Second, the absorption loss can take place inside the sections of the crystal usually left undoped for the mechanical assembly of the crystal inside water cooling camera, and also inside the Q-switch. For instance, in near IR region undoped YAG has linear absorption coefficient $\alpha\approx1.5x10^{-3}$ cm^{-1}. Assuming similar absorption for ≈2.1 μm radiation one finds that for 4 cm of undoped YAG sections $2\sum_i\alpha_i l_i\approx0.012$ and about 10% loss in G-pulse.

Third, the effect of two-photon absorption which may have a serious effect on G-pulse generation when the laser power attains MW level. In particular, in general case the absorption loss inside optical medium is defined by the following equation including linear and non-linear (two-photon) absorption as:

$$dI/dz=-\alpha I-\beta I^2, \tag{27}$$

where the value β is known to be within the range of 10^{-11}-10^{-9} cm/W for wide range of optical materials (Dmitriev *et al*., 1997).

This equation suggests that the effect of two-photon absorption is significant when $\alpha\approx\beta I$. In particular, for the undoped YAG sections this takes place when $\beta I\approx\alpha\approx0.0015$cm^{-1}. Let us estimate the possible range for βI assuming that the target level of pulse energy should attain the level of $Q\approx0.1$ J with pulse width of $\tau_p\approx500$ ns. This gives us maximal power inside the cavity of $P=Q/\tau_p=0.1$ J/ 500 ns= $2x10^5$ W. The maximal intensity in the laser beam will be $I=P/\pi\ r_0^2\approx0.65x10^7$ W/cm² (where $r_0\approx0.1$ cm is the laser beam radius). Thus, one obtains for $\beta I\approx10^{-11}$-10^{-9} cm/W x $0.65x10^7$ W/cm²=6.5x(10^{-5} -10^{-3}) cm^{-1}, which shows that the effect of two-photon absorption may be similar and even higher than that of linear absorption $\alpha\approx1.5x10^{-3}$ cm^{-1}. Moreover, in experiments with shorter cavity and shorter pulse width this effect may become even more significant. In particular, 500 ns pulses correspond to the cavity length of 3 m. In case of 1 m cavity the pulse duration shortens to the level of ≈100-200 ns, and the maximal power achieves the level of $P\approx1$ MW. Thus, for increased intensity

one gets $\beta I \approx 3.25x(10^{-4} - 10^{-2})$ cm^{-1},which shows that the two-photon absorption may be an order of magnitude higher than that of linear absorption, $\alpha \approx 1.5x10^{-3}$ cm^{-1}.
Additionally one should pay attention to the possible interference of two-photon absorption loss with the output transmittance T_{out}. The above computational model shows that the increase in T_{out} shortens G-pulse width tending to increase its peak power. In fact, the possible involvement of the two-photon absorption can inhibit this effect decreasing G-pulse energy. We should also note that the simulation of the effect of two-photon absorption requires formal correction of Eq. (8) by introduction of an additional loss term $\propto \beta\Phi_0^2$.

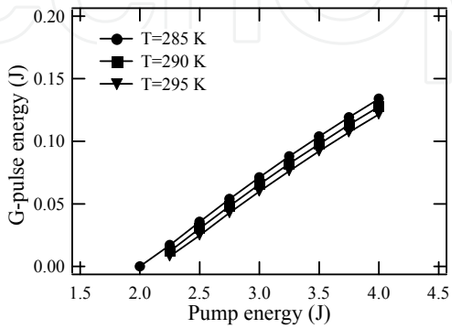

Fig. 14. G-pulse energy versus pumping energy for the experimental conditions by Yu *et al*. 1998.

6.2 Tm,Ho:YLF

For this case the rate dynamics equation and related parameters are fully specified by Walsh *et al*. 2004. The model was verified by using the set of experimental condition reported by Yu *et al*., 1998 for the development of Q-switched 125 mJ Tm,Ho:YLF laser using ≈790 nm LD pulse of 1.2 ms duration for side-pumping of 2 cm long 4 mm diameter crystal rod set up in 3.3 m cavity with T_{out}=0.18 for the output mirror. Results of our simulations performed for this particular case are given in Fig. 14 where the resulting G- pulse energy is given versus the pumped energy for T=285, 290 and 295 K. The simulations show a good agreement with the experimental data (Yu *et al*., 1998). In particular, 4 J pumping gives the output energy of about ≈0.14 J for T=285 K and ≈0.13 J for T=290 K, correspondingly. The experiment shows ≈0.125 J for T=292 K (Yu *et al*., 1998). The pulse generation threshold is computationally found to be near the pumping energy of 2 J which is also close to the value of the extrapolated experimental data (Yu *et al*., 1998). Additionally, the simulation data given in Fig. 14 shows that the G-pulse energy strongly depends on the operating temperature. For instance, for 4 J pump the temperature increase from 285 K to 295 K is found to decrease G-pulse energy on ≈15%.
In Fig. 15 we show (a) G-pulse power versus time for several pumping energies, (b) G-pulse power versus time for various photon injection seeder power and (c) G-pulse width versus pumping energy. The pulse width shows decrease with the increase of the pumping energy similar to the experimental data. However, the values of pulse width found in our simulation is about 2 times higher that those of experimental study (Yu *et al*., 1998). The seeder does not significantly change the pulse width, and shortens the time between the moment of Q-switch opening and G-pulse generation.

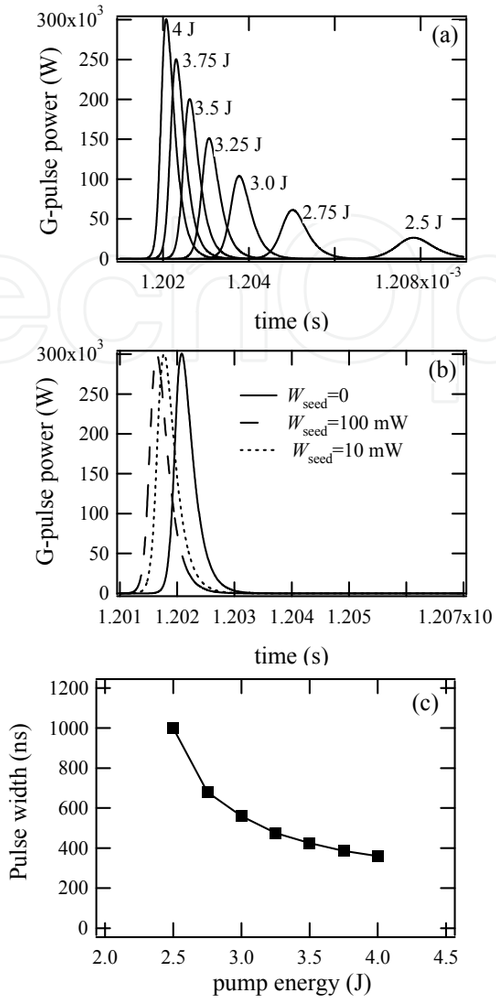

Fig. 15. G-pulse power versus time for (a) for different pump energy, (b) constant pump energy 4 J and photon seeder powers, and (c) pulse width versus the pump energy for experimental conditions by Yu *et al*. 1998.

6.3 Tm,Ho:YAG

In the case of Tm,Ho:YAG serious simplifications can be done allowing model reduction to two rate equations describing the electron density at the excited levels $^3F_4$ and $^5I_7$, and ground state levels $^3H_6$ and $^5I_8$ assuming that the excitation is rapidly transferred from $^3H_4$ to $^3F_4$ level. In particular, this model based on 4-level rate dynamics model (Bruneau, *et al*. 1998) is given by the set of equations:

$$\frac{dn_2}{dt} = R_p(t) - \frac{n_2}{\tau_2} - p_{28} n_2 n_8 + p_{71} n_7 n_1 , \tag{28}$$

$$\frac{dn_7}{dt} = -\frac{n_7}{\tau_7} - p_{27} n_2 n_7 + p_{28} n_2 n_8 - p_{71} n_7 n_1 - \frac{c\sigma_{se}}{\eta}(f_7 n_7 - f_8 n_8)\phi_0(t,\mathbf{r}) , \tag{29}$$

where $n_1 \approx n_{Tm}$-n_2, $n_8 \approx n_{Ho}$-n_7, p_{28}=31.7x10^{-17} cm^3/s, p_{71} =0.09p_{28}, p_{27}=7.24x10^{-17} cm^3/s are the probabilities of the optical transitions, τ_2=11 ms and τ_7=15.6 ms are the level lifetimes, σ_{se}=9.2x10^{-20} cm^2 is the stimulated emission cross-section, f_7=0.104 and f_7=0.018 are the Boltzmann populations factors for T=20 ^{0}C.

The experimentally measured and simulated normal pulse energy versus pumping energy is shown in Fig. 16 (a) and (b). The experiments were done using two crystal set of Tm (6%), Ho (0.4 %): ceramic YAG of 3 mm in diameter and 22 mm long doped zone (within the rod of 70 mm in length). Output cavity transmission is T_{out}=0.15, and cavity length is L_{cav}=40 cm. The temperature and humidity inside the dehumidified box of 30 cm in length was 24.8 ^{o}C and H=0.029 (2.9 %), correspondingly. The temperature and humidity outside the dehumidified box was 25.2 ^{o}C and H=0.42 (42 %), correspondingly. The total loss inside the cavity was estimated for laser beam waist is 1.5 mm and loss inside the undoped YAG sections as $2\sum_i \alpha_i l_i$ =0.034.

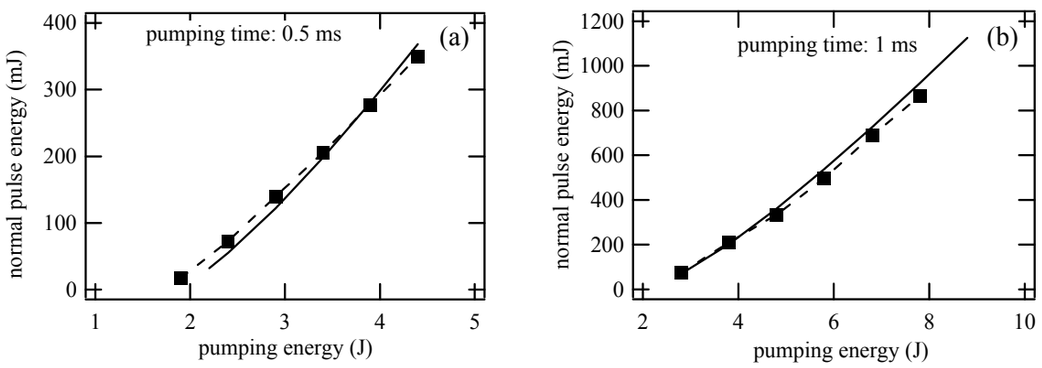

Fig. 16. Normal pulse energy versus pumping energy: solid line – computational, broken line – experiments: (a) pumping time 0.5 ms and (b) pumping time 1.0 ms.

In Fig. 17 we show experimentally measured and simulated normal pulse power versus time made for the same crystal set, cavity length of 100 cm with the temperature of 22 ^{0}C and humidity H=0.36 (36 %) (T_{out}=0.15). Pumping time is 1 ms. Fig. 17 (a) shows very good agreement of the experimental and simulated pulse power versus time. However, the careful comparison shows several discrepancies which may be attributed to a difficulties in defining precise experimental conditions. Nevertheless, all time scales of pulse generation in Fig. 17 (a) and (b), including relaxation period of ≈0.2 ms, agree well with each other.

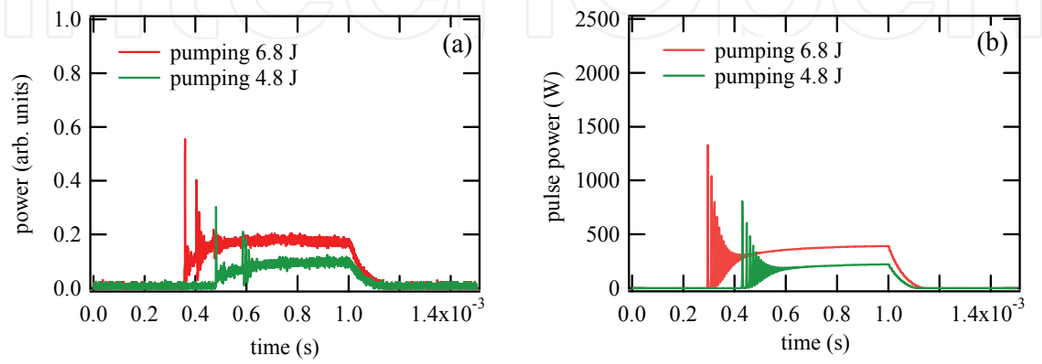

Fig. 17. Normal pulse power versus time (a) experiment and (b) simulation.

It is worth noting that experimental and simulated results show output power stabilization after several dozens of relaxation spikes agreeing with previous analytical derivations by Elder and Payne, 1995.

7. Summary and conclusions

Complex thermo-optical model for simulation and optimization of 2 μm co-doped Tm,Ho solid state lasers is developed based on (i) 8-levels rate dynamics model for the excitation transfer to Ho^{3+} ions from LD pumped Tm^{3+} ions and (ii) the oscillator energy equation with TEM_{00} distribution for stimulated photons inside the laser cavity. This optical model is rigourosly coupled with two-dimensional time dependent heat transfer model including absorption, heat release and heat transfer inside the operating crystal, as well as thermal effect of spontaneously emitted infrared radiation fluxes. In the case of water cooled laser operation these IR radiations fluxes are shown to be fully absorbed within the water boundary layer of several hundreds microns and to produce a significant inhibition of heat dissipation from the operating crystal. In particular, in case of water cooled operation only ≈40 % of the pumped energy is transformed into the heat directly inside the crystal, whereas ≈45 % is IR radiation spontaneously emitted by $^3H_4$, $^3H_5$, $^3F_4$ and $^5I_7$ levels and fully absorbed by water within the thermal boundary layer. This model is used in simulations for a wide range of parameters for 780 nm LD side-pumped co-doped Tm,Ho:YLF and YAG lasers. Two significant effects are found for the particular case of Q-switched high repetition (20-50 Hz) Tm,Ho:YLF laser operation with output pulse energy ≈0.1 J and ≈500 ns pulse duration. First, for obtaining a giant (G) pulse from a 2.06 μm solid state Tm,Ho:YLF laser by the active Q-switching technique, the optimal Ho concentration will be higher than that used in normal operation. In simulations of 500 ns G-pulse generation maximal efficiency occurred at 6 % Tm and 1.0 % Ho, in contrast with 0.4% Ho found to be optimal for the normal pulse generation. Maximal energy output from Tm,Ho:YLF lasers can be achieved by incorporating a delay of about 0.7 ms between 0.5 ms 780 nm LD pulsed pumping and the start of Q-switched G-pulse operation. Secondly, simulation suggests that the ≈0. 7 ms delay after 0.5 ms LD pumping pulse should be used for retrieving the maximum of the pumped energy. Finally, heat transfer effects are analyzed in detail showing output pulse energy decrease for high repetition rates due to temperature influence on the upper and lower level population factors.

8. Acknowledgements

This work was supported by the National Institute of Information and Communications Technology (Japan). We would also like to thank Dr. J. Hester from the Australian Nuclear Science and Technology Organization for numerous valuable comments.

9. References

Akhmanov, S. A.; Khokhlov, R. V. & Sukhorukov, A. P., *Self-focusing, self-defocusing and self-modulation of laser beams*, Laser Handbook, V.2. Eds. F. T. Arecchi, E. O. Schulz-Dubois, North-Holland, Amsterdam 1972. 978-0720402131

Alpat'ev, A. N.; Smirnov, V. A. & Shcherbakov, I. A. (1998). Relaxation oscillations of the radiation from a 2-μm holmium laser with a Cr,Tm,Ho:YSGG crystal. *Quantum Electronics,* Vol. 28, No. 2, 143-146, 1063-7818(print); 1468-4799(online)

Barnes, N. P.; Filer, E. D.; Morison, C. A. & Lee, C. J. (1996). Ho:Tm Lasers: Theoretical. *IEEE Journal of Quantum Electronics,* Vol. 32, No. 1, 92-103, 0018-9197

Bourdet, G. L. & Lescroart, G. (1999). Theoretical modeling and design of a Tm, Ho: $YLiF_4$ microchip laser. *Applied Optics*, Vol. 38, No. 15, 3275-3281, 0003-6935(print); 1539-4522(online)

Bruneau, D.; Delmonte, S. & Pelon, J. (1998). Modeling of Tm, Ho: YAG and Tm, Ho: YLF 2-μm lasers and calculation of extractable energies. *Applied Optics*, Vol. 37, No. 36, 8406-8419, 0003-6935(print); 1539-4522 (online)

Černý, P. & Burns, D. (2005). Modeling and experimental investigation of a diode-pumped Tm:$YAlO_3$ laser with *a-* and *b-* cut crystal orientations. *IEEE Journal of Selected Topics in Quantum Electronics*, Vol. 11, No. 3, 674-681. 1077-260X

Dmitriev, V. G.; Gurzadyan, G. G. & Nikogosyan, D. N. (1997). *Handbook of Nonlinear Optical Crystals 2nd Edition*, Springer-Verlag, 3-540-61275-0, Berlin

Eichhorn, M. (2008). Quasi-three-level solid-state lasers in the near and mid infrared based on trivalent rare earth ions. *Applied Physics B,* Vol. 93, No. 2-3, 269-316, 0946-2171 (print); 1432-0649 (online)

Elder, I. F. & Payne, M. J. P. (1995). Lasing in diode-pumped Tm:YAP, Tm,Ho:YAP and Tm,Ho,YLF. *Optical Communications,* Vol. 145, No. 1-6, 329-339, 0030-4018

French, V. A.; Petrin, R. R.; Powell, R. C. & Kokta, M. (1992). Energy-transfer processes in Y3Al5O12:Tm, Ho. *Physical Review B,* Vol. 46, No. 13, 8018-8026, 1098-0121(print); 1550-235X(online); 1538-4489(CD-Rom)

Galzerano, G.; Sani, E.; Toncelli, A.; Della Valle, D.; Taccheo, S.; Tonelli, M. & Laporta, P. (2004). Widely tunable continuous-wave diode-pumped 2-μm Tm-Ho:KYF_4 laser. *Optics Letters*, Vol. 29, No. 7, 715-717, 0146-9592(print); 1539-4794(online)

Izawa, J.; Nakajima, H.; Hara, H.; & Arimoto, Y. (2000). Comparison of lasing performance of Tm,Ho:YLF lasers by use of single and double cavities. *Applied Optics,* Vol. 39, No. 15, 2418-2421, 0003-6935(print); 1539-4522(online)

Jackson, S. D. & King, T. A. (1998). CW operation of a 1.064-μm pumped Tm-Ho-doped silica fiber laser. *IEEE Journal of Quantum Electronics,* Vol. 34, No. 9, 1578-1587, 0018-9197

Jani, M. G.; Reeves, R. J.; Powell, R. C.; Quarles, G. J. & Esterovitz, L. (1991). Alexandrite-laser excitation of a Tm:Ho:$Y_3Al_5O_{12}$ laser. *Journal of the Optical Society of America B,* Vol. 8, No. 4, 741-746, 0740-3224(print); 1520-8540(online)

Jani, M. G.; Naranjo, F. L.; Barnes, N. P.; Murray, K. E. & Lockard, G. E. (1995). Diode-pumped long-pulse-length Ho:Tm:$YLiF_4$ laser at 10 Hz. *Optics Letters,* Vol. 20, No. 8, 872-874, 0146-9592(print); 1539-4794(online)

Koechner, W. (2006). *Solid-State Laser Engineering 6th Edition*, Springer, 978-0387290942, New York

Lee, C. J.; Han, G. & Barnes, N. P. (1996). Ho:Tm Lasers: Experiments. *IEEE Journal of Quantum Electronics,* Vol. 32, No. 1, 104-111, 0018-9197

Louchev, O. A.; Urata, Y. & Wada, S. (2007). Numerical simulation and optimization of Q-switched 2 μm Tm, Ho:YLF laser. *Optics Express,* Vol. 15, No. 7, 3940-3947, 1094-4087

Louchev, O. A.; Urata, Y.; Saito, N; & Wada, S. (2007). Computational model for operation of 2 μm co-doped Tm, Ho solid-state lasers. *Optics Express,* Vol. 15, No. 19, 11903-11912, 1094-4087

Louchev, O. A.; Urata Y.; Yumoto, M.; Saito, N.; & Wada, S. (2008). Thermo-optical modeling of high power operation of 2 μm co-doped Tm,Ho solid-state lasers. *Journal of Applied Physics,* Vol. 104, No. 3, 033114-033114-9, 0021-8979(printed); 1089-7550(online)

Petrin, R. R.; Jani, M. G.; Powell, R. C. & Kokta, M. (1992). Spectral dynamics of laser-pumped $Y_3Al_5O_{12}$:Tm, Ho lasers. *Optical Materials,* Vol. 1, No. 2, 111-124, 0925-3467

Risk, V. P. (1988). Modeling of longitudinally pumped solid-state lasers exhibiting reabsorption losses. *Journal of the Optical Society of America B,* Vol. 5, No. 7, 1412-1423, 0740-3224(print); 1520-8540(online)

Rustad, G. & Stenersen, K. (1996). Modeling of laser-pumped Tm and Ho lasers accounting for upconversion and ground-state depletion. *IEEE Journal of Quantum Electronics,* Vol. 32, No. 9, 1645-1656, 0018-9197

Sato, A.; Asai, K. & Mizutani, K. (2004). Lasing characteristics and optimizations of diode-side-pumped Tm,Ho:$GdVO_4$ laser. *Optics Letters,* Vol. 29, No. 8, 836-838, 0146-9592(print); 1539-4794(online)

Sudesh, V. & Asai, K. (2003). Spectroscopic and diode-pumped-laser properties of Tm,Ho:YLF; Tm,Ho:LuLF; and Tm,Ho:LuAG crystals: a comparative study. *Journal of the Optical Society of America B,* Vol. 20, No. 9, 1829-1837, 0740-3224(print); 1520-8540(online)

Tyminski, J. K.; Franich, D. M. & Kokta, M. (1989). Gain dynamics of Tm,Ho:YAG pumped in near infrared. *Journal of Applied Physics,* Vol. 65, No. 8, 3181-3188, 0021-8979(printed); 1089-7550(online)

Walsh, B. M. (2009). Review of Tm and Ho materials; spectroscopy and lasers. *Laser Physics*, Vol. 19, No. 4, 855-866, 1054-660X(print); 1555-661(online)

Walsh, B. M.; Barnes, N. P.; Petros, M.; Yu, J. & Singh, U. N. (2004). Spectroscopy and modeling of solid state lanthanide lasers: application to trivalent Tm^{3+} and Ho^{3+} in $YLiF_4$ and $LuLiF_4$. *Journal of Applied Physics,* Vol. 95, No. 7, 3255-3271, 0021-8979(print); 1089-7550(online)

Wieliczka, D. M.; Weng, S. & Querry, M. R. (1989). Wedge shaped cell for highly absorbent liquids: infrared optical constants of water. *Applied Optics,* Vol. 28, No. 9, 1714-1719, 0003-6935(print); 1539-4522(online)

Yu, J.; Singh, U. N.; Barnes, P. & Petros, M. (1998). 125-mJ diode-pumped injection-seeded Ho:Tm:YLF laser. *Optics Letters*, Vol. 23, No. 10, 780-782, 0146-9592(print); 1539-4794 (online)

Yu, J.; Trieu, B. C.; Modlin, E. A.; Singh, U. N.; Kavaya, M. J.; Chen, S.; Bai, Y.; Petzar, P. J. & Petros, M. (2006). 1 J/pulse Q-switched 2 μm solid-state laser. *Optics Letters*, Vol. 31, No. 4, 462-464, 0146-9592(print); 1539-4794(online)

Zhang, X.; Ju, Y. & Wang, Y. (2006). Theoretical and experimental investigation of actively Q-switched Tm,Ho:YLF lasers. *Optics Express*, Vol. 14, No. 17, 7745-7750, 1094-4087

Advances in Solid State Lasers Development and Applications

Edited by Mikhail Grishin

ISBN 978-953-7619-80-0
Hard cover, 630 pages
Publisher InTech
Published online 01, February, 2010
Published in print edition February, 2010

Invention of the solid-state laser has initiated the beginning of the laser era. Performance of solid-state lasers improved amazingly during five decades. Nowadays, solid-state lasers remain one of the most rapidly developing branches of laser science and become an increasingly important tool for modern technology. This book represents a selection of chapters exhibiting various investigation directions in the field of solid-state lasers and the cutting edge of related applications. The materials are contributed by leading researchers and each chapter represents a comprehensive study reflecting advances in modern laser physics. Considered topics are intended to meet the needs of both specialists in laser system design and those who use laser techniques in fundamental science and applied research. This book is the result of efforts of experts from different countries. I would like to acknowledge the authors for their contribution to the book. I also wish to acknowledge Vedran Kordic for indispensable technical assistance in the book preparation and publishing.

InTech Europe
University Campus STeP Ri
Slavka Krautzeka 83/A
51000 Rijeka, Croatia
Phone: +385 (51) 770 447
Fax: +385 (51) 686 166
www.intechopen.com

InTech China
Unit 405, Office Block, Hotel Equatorial Shanghai
No.65, Yan An Road (West), Shanghai, 200040, China
中国上海市延安西路65号上海国际贵都大饭店办公楼405单元
Phone: +86-21-62489820
Fax: +86-21-62489821

IntechOpen